

Design and optimisation of a turbofan blade filled with Multi-Poisson's Ratio Soft–Hard integrated structures

Peijie Sun and Weizhu Yang* 

School of Mechanics and Transportation Engineering, Northwestern Polytechnical University, Xi'an 710129, PR China

Received: 2 November 2025 / Accepted: 9 December 2025

Abstract. This paper introduces a bioinspired design and optimisation methodology for wide-chord hollow turbofan blades filled with graded soft-hard architected materials to improve bird-strike survivability while retaining aerodynamic performance. A Multi-Poisson's Ratio Soft-Hard (MPRSH) infill design concept was developed in which negative and positive lattices and soft matrix regions are distributed spanwise according to the equal-strength design philosophy. Numerical models were constructed in which the blade was discretised into shell and solid finite elements, bird impact was modelled using Smoothed Particle Hydrodynamics (SPH), and metal damage was described using the Johnson-Cook model. Design optimisation was proceeded in two stages — parametric sampling and Kriging surrogate construction for lattice metamaterial proportioning, followed by surrogate-assisted evolutionary optimisation of regional wall thicknesses. Surrogate-assisted optimisation produced an initial lightweight design 35% lighter than a solid baseline. A refined final design that weighs 18% less than the baseline. Bird-strike simulations show that PA cores produce highly localised stress/plasticity in small-bird impacts, while rubber fillers limit local plasticity but may fail under large-bird loading. An improved hybrid further reduces displacement and maximum stress. Results indicate that Poisson-ratio mismatch enables adaptive deformation and reduced energy transfer, demonstrating promising applications of graded multi-material infills for future fan blades.

Keywords: Turbofan blade / infill structure / soft-hard integration / Poisson's ratio / design optimisation

1 Introduction

The commercial aero-gas turbine, first realised as a practical technology in the 1930s, has evolved into the dominant propulsion system for modern civil aviation and an important source of industrial power generation [1–5]. Despite remarkable advances in efficiency, reliability, and overall performance, foreign-object damage (FOD)—particularly bird ingestion—remains one of the most persistent and hazardous threats to engine safety. Statistical analyses indicate that a substantial portion of severe bird-strike events in civil aircraft involve engine ingestion, which can cause serious fan-blade damage and, in extreme cases, result in in-flight engine failure [6–9]. As turbofan engines continue to trend toward higher loadings, larger diameters, and greater thrust-to-weight ratios, the mechanical demands placed on the fan stage become increasingly stringent. Ensuring that fan blades can sustain high aerodynamic loading while simultaneously resisting

impact events such as bird strikes has therefore become a key engineering challenge.

To meet these competing requirements, contemporary high-bypass turbofan engines widely adopt wide-chord hollow fan blades. These blades offer several advantages over conventional solid designs, including improved aerodynamic efficiency, reduced structural mass, and enhanced fatigue performance [10]. However, the transition to hollow configurations introduces new structural challenges. Simple internal cavities often do not provide the mechanical strength, stiffness, or impact resistance required under realistic engine operating conditions. As a result, modern blade designs frequently incorporate engineered internal architectures or filler materials to augment mechanical performance [11]. Filled or reinforced cavity structures can absorb impact energy more effectively, as the filler deforms plastically or elastically during a strike, redistributing loads and delaying localised failure. Consequently, cavity filling has become increasingly common in wide-chord hollow fan blades, enabling designers to balance aerodynamic performance with improved impact tolerance [12].

* e-mail: wzhyang@nwpu.edu.cn

A growing body of research has focused on optimising hollow-blade infill strategies for enhanced bird-strike resistance. Zeng et al. [13] conducted structural optimisation of hollow blades using explicit bird-strike analysis to identify interior configurations that improve energy absorption. Zhang et al. [14] examined lattice, foam, and hybrid lattice-foam cores, demonstrating that appropriately designed cellular architectures can significantly enhance the impact resistance of composite panels. Giannaros et al. [15] analysed composite foam-filled curved panels under bird-strike loading and proposed both high- and low-fidelity predictive models for damage estimation. Yan et al. [16] developed a spatially graded lattice filling technique for curved plates, validating its effectiveness through numerical simulation and experiments. Hedayati et al. [17] investigated foam-filled structures with varying densities and internal panel configurations, providing further guidance for designing infills under equal-thickness constraints. Although highly insightful, these studies mainly consider relatively simple or single-material architectures, limiting the degree of performance tuning achievable through geometry alone.

In parallel, metamaterial research—particularly on auxetic structures with negative Poisson’s ratios—has opened promising new pathways for impact protection. Auxetic materials expand laterally when stretched and contract when compressed, enabling unique deformation modes that enhance energy absorption and improve resistance to shear and indentation. Zhu et al. [18] introduced an extendable assembled auxetic honeycomb (EAAH) formed by interlocking slotted corrugated plates. This modular design provides significant mechanical tunability, facilitating low peak crush stress while maintaining excellent structural stability under dynamic loading. Both the extendable and non-extendable versions outperform conventional integrated auxetic honeycombs (IAH), although the increased flexibility slightly reduces collapse stress [19]. Lu et al. [20] proposed a three-dimensional “tetra-missing-rib” auxetic meta-structure exhibiting coupled tension-torsion deformation, demonstrating that both stiffness and Poisson’s ratio can be tuned over a wide range via geometric design. Wei et al. [21] investigated 3D assembled auxetic structures with compression-twisting coupling to evaluate their energy absorption characteristics under different loading scenarios. Collectively, these studies illustrate the potential of assembled auxetic meta-structures to achieve high energy absorption, programmable mechanical properties, and modular manufacturability. Additional work, such as Zhang et al.’s windmill-shaped metamaterials exhibiting negative thermal expansion (NTE), further highlights the increasing sophistication of multifunctional meta-structure design [22].

Beyond synthetic metamaterials, biological systems provide powerful inspiration for designing structures that combine high strength, exceptional toughness, and efficient energy dissipation. Natural composites such as bone, nacre, conch shell, and the Bouligand structures of the stomatopod dactyl club achieve extraordinary resilience by integrating stiff and compliant phases across multiple hierarchical length scales [23–30]. These architectures

promote crack deflection, stress redistribution, and multi-scale energy dissipation despite significant mechanical mismatches between constituent materials [31–34]. With recent advances in multi-material additive manufacturing, it has become increasingly feasible to recreate such hierarchical and spatially graded microstructures in engineered systems [35–37]. Applying these bioinspired principles to fan-blade design offers a promising route to achieving lightweight construction while simultaneously increasing impact tolerance and damage resistance.

Building upon these developments and our prior work on multi-Poisson’s-ratio soft-hard integrated structures [38], this study presents a novel Multi-Poisson’s Ratio Soft-Hard Filled (MPRSHF) turbofan blade. This design integrates spatially graded soft and hard materials arranged to achieve tailored Poisson’s-ratio responses across the blade interior. By combining bioinspired hierarchical arrangements with an optimisation-driven design framework, the proposed MPRSHF infill architecture provides enhanced impact energy absorption, improved mechanical robustness, and reduced structural mass—all without compromising aerodynamic or operational performance. The results demonstrate that multi-material, functionally graded infills can play a transformative role in next-generation turbofan blade design, offering a pathway toward safer, lighter, and more damage-tolerant aero-engine components.

2 Structure design

Previous studies [10,13,39] have shown that, under applied loading the region of maximum stress is located at the blade root—particularly near the trailing edge—because the radial direction does not generally coincide with the blade stacking line. Our earlier work [38] demonstrated that a deliberate mismatch in Poisson’s ratio between adjacent materials can improve bulk mechanical performance. Building on this principle, the present study exploits Poisson-ratio contrast to enhance blade stiffness and strength: when a negative-Poisson-ratio laminate is paired with a positive-Poisson-ratio laminate, the auxetic layer bends toward the positive layer under tensile loading, producing a tension-bending coupling that improves load distribution.

Figure 1 schematises the Multi-Poisson-Ratio Soft-Hard-Filled (MPRSHF) turbofan blade. The interior is partitioned spanwise into three principal regions (twelve subregions total) and infilled with architected lattices and a compliant matrix. Cavities employ TC4 lattices with Poisson’s ratios of approximately +0.4 and −0.8, embedded in a soft matrix (polyamide or rubber). The central spanwise region forms the primary load-bearing spar and carries centrifugal (tensile), bending and torsional loads; it uses a hybrid infill (both auxetic and conventional TC4 lattices integrated with the soft matrix) to tailor stiffness and strength. Profile-edge subregions use the auxetic lattice to increase local impact energy absorption, while the trailing region is filled with a low-density compliant matrix to save mass and preserve the external aerodynamic surface. An equal-strength optimisation strategy selects

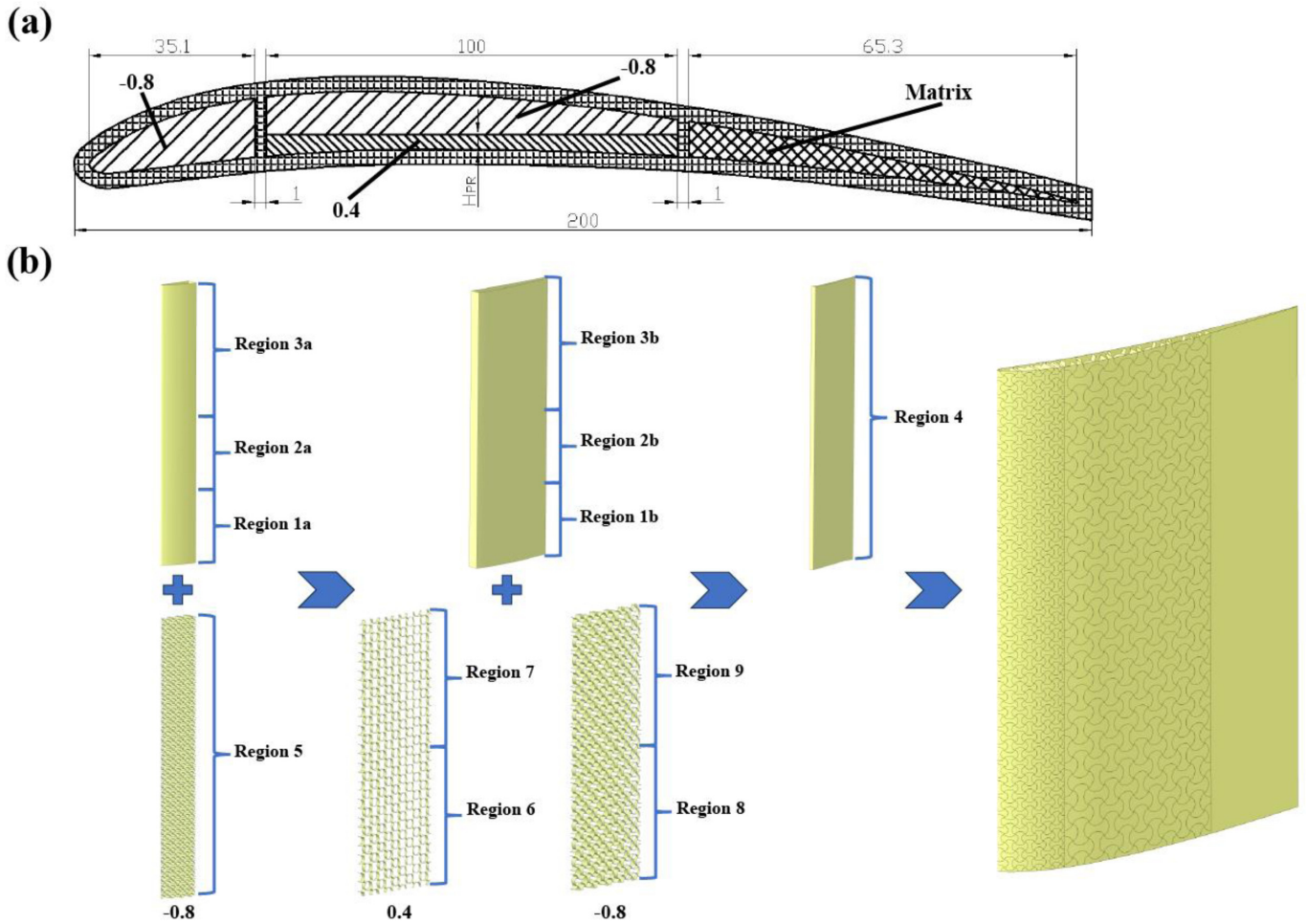


Fig. 1. MPRSHF turbfan-blade concept. (a) Blade profile. (b) Three main spanwise infill regions: profile-edge auxetic lattice ($\nu \approx -0.8$) for impact resistance; central spar (primary load-bearing); trailing compliant fill for mass saving.

regional reinforcement and the spatial distribution of Poisson’s ratios so that tensile stresses from rotation help counteract bending from dynamic loads, thereby mitigating twist and balancing impact survivability, stiffness and blade mass.

3 Modelling and optimisation

3.1 The blade model

The outer wall and the infill hard lattice of the blade were meshed using four-node and three-node shell elements (S4R and S3R), while the soft matrix core was meshed with eight-node linear hexahedral hybrid elements (C3D8IH). The lattice infill was embedded within the soft matrix using the embedded element technique to ensure consistent deformation compatibility between the two materials. The final finite element model of the blade comprised 4,743 solid nodes and 2,500 solid elements, along with 123,794 shell nodes and 108,993 shell elements, as shown in Figure 2b.

The blade root was fixed. A surface pressure load was applied to the affected area of the blade, and centrifugal loading due to rotation (1,500 rpm) was applied to the entire blade as a body force (implemented via a prescribed rotational velocity about the shaft axis).

3.2 Blade material model

The blade wall panels and the lattice metamaterial infill were fabricated from TC4 (Ti-6Al-4V), while the soft matrix is PA and rubber. The material parameters for TC4, PA and rubber are listed in Tables 1,2 and 3, respectively.

The Johnson-Cook plasticity model [43] was employed to represent rate- and temperature-dependent plastic flow. This phenomenological model is a von Mises-type plasticity formulation with an analytical isotropic hardening law and explicit strain-rate and thermal dependence. The Johnson-Cook flow stress (static yield stress), σ^0 , is given by

$$\sigma^0 = [A + B(\bar{\epsilon}^{pl})^n](1 - \hat{\theta}_{\text{Plasticity}}^m) \quad (1)$$

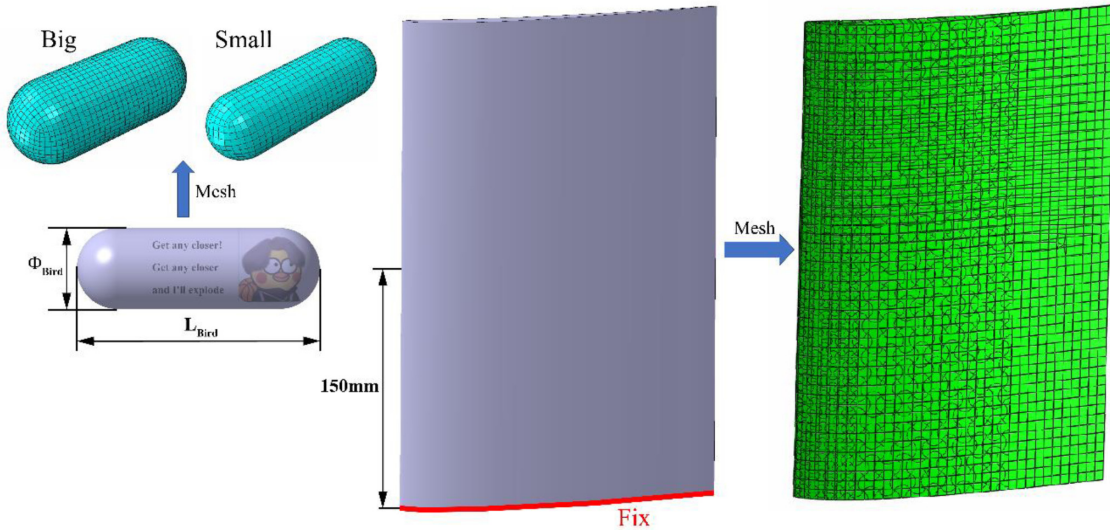


Fig. 2. Numerical simulation model for bird strike of the turbofan blade. (a) Geometric model and boundary conditions, (b) Finite element model of the turbofan blade.

Table 1. Parameters of the TC4 [40].

Density (t/mm^3)	Elastic modulus (MPa)	Poisson's ratio	Yield stress (MPa)
4.43e-09	1.11e5	0.34	895

Table 2. Parameters of the PA [41].

Density (t/mm^3)	Elastic modulus (MPa)	Poisson's ratio	Damage stress (MPa)
1.12e-09	1.50e3	0.394	57

where $\bar{\epsilon}^{pl}$ is the equivalent plastic strain and A , B , n , and m are material parameters. $\hat{\theta}_{Plasticity}$ is the nondimensional temperature defined as

$$\hat{\theta}_{Plasticity} \equiv \begin{cases} 0 & , \theta < \theta_{transition, Plasticity} \\ (\theta - \theta_{transition, Plasticity}) / (\theta_{melt} - \theta_{transition, Plasticity}) & , \theta_{transition, Plasticity} \leq \theta \leq \theta_{melt} \\ 1 & , \theta > \theta_{melt} \end{cases} \quad (2)$$

where θ is the current temperature, θ_{melt} is the melting temperature, the $\theta_{transition, Plasticity}$ is the transition temperature defined as the one at or below which there is no temperature dependence on the expression of the yield stress. The material parameters A , B , and n must be measured at or below the transition temperature. The material parameter m should be determined based on measurements above the transition temperature.

The parameters of the Johnson-Cook plasticity model are listed in Table 4.

The Johnson-Cook model [31] was used to describe ductile damage in the analysis. In Abaqus/Explicit, the Johnson-Cook damage criterion is implemented as a special case of the ductile-damage formulation in which the equivalent plastic strain at damage initiation, $\bar{\epsilon}_D^{pl}$, is given by

$$\bar{\epsilon}_D^{pl} = [d_1 + d_2 \exp(-d_3 \eta)] \left[1 + d_4 \ln \left(\frac{\dot{\epsilon}}{\dot{\epsilon}_0} \right) \right] (1 + d_5 \hat{\theta}_{Damage}) \quad (3)$$

where d_1 – d_5 are failure parameters and $\dot{\epsilon}_0$ is the reference strain rate. $\hat{\theta}_{Damage}$ is the nondimensional temperature defined as

$$\hat{\theta}_{Damage} \equiv \begin{cases} 0 & , \theta < \theta_{transition, Damage} \\ (\theta - \theta_{transition, Damage}) / (\theta_{melt} - \theta_{transition, Damage}) & , \theta_{transition, Damage} \leq \theta \leq \theta_{melt} \\ 1 & , \theta > \theta_{melt} \end{cases} \quad (4)$$

where θ is the current temperature, θ_{melt} is the melting temperature, the $\theta_{transition, Damage}$ is the transition temperature defined as the one at or below which there is no temperature dependence on the expression of the damage strain $\bar{\epsilon}_D^{pl}$. The material parameters must be measured at or below the transition temperature.

When the Johnson-Cook damage model is employed together with the Johnson-Cook plasticity model, the melting and transition temperatures specified for damage must be consistent with those defined in the plasticity material definition. The Johnson-Cook damage-initiation criterion may be used concurrently with other initiation criteria (for example, ductile or shear criteria); Abaqus

Table 3. Parameters of the rubber [42].

μ_1	μ_2	μ_3	α_1	α_2	α_3	Strength (MPa)
1.90	-1.92e-10	3.19e-4	1.06	-17.7	12.38	3.1

Table 4. The parameters of the Johnson-Cook plasticity model [40].

A (MPa)	B (MPa)	C	$\bar{\epsilon}^{\text{pl}}$ (s^{-1})	θ_{melt} (K)	n	m
1060	1090	1.17e-2	4e-4	1878	8.84e-1	1.1

Table 5. Failure parameters of the Johnson-Cook model [40].

d_1	d_2	d_3	d_4	d_5
-9.00e-2	2.70e-1	4.80e-1	1.40e-2	3.87

evaluates each initiation criterion independently. Once an initiation criterion is satisfied, damage accumulation proceeds according to the chosen damage-evolution law for that criterion. The failure parameters are listed in Table 5.

3.3 Computational model

During impact, the stresses developed within the bird model greatly exceed the bird tissue strength, causing the bird to behave in a fluid-like manner; therefore, bird impact is commonly simulated using hydrodynamic approaches. In this study, the bird body was discretised using the smoothed-particle hydrodynamics (SPH) method [44,45], which naturally handles large deformations, fragmentation and severe mesh distortion that occur during high-velocity impacts. The equation of state (EOS) defines the thermodynamic relationship among density, internal energy, temperature, volume (or compression) and pressure. In continuum impact simulations, the pressure P is therefore modelled as a function of density and internal energy,

$$P = P(V, E) = P(V, T) \quad (5)$$

where V , E , T are volume, internal energy, and temperature, respectively.

A frequently used practical form is the Mie-Grüneisen EOS, written in the form

$$P - P_H = \Gamma(E_m - E_H) \quad (6)$$

$$\Gamma = \Gamma_0 \frac{\rho_0}{\rho} \quad (7)$$

$$E_H = \frac{P_H \eta}{2\rho_0} \quad (8)$$

Table 6. The parameters of $U_s - U_p$ EOS [40].

c_0 (m/s)	s	Γ_0	ρ_0 (kg/m^3)
1.45e2	0	0	9.832e2

where P_H is Hugoniot pressure, E_H is Hugoniot energy, Γ_0 is parameter of the material, and ρ_0 is the reference density, $\eta = 1 - \frac{\rho_0}{\rho}$.

The linear $U_s - U_p$ Rankine-Hugoniot relation is expressed as

$$P_H = \frac{\rho_0 c_0^2 \eta}{(1 - s\eta)^2} \quad (9)$$

where c_0 is the reference sound speed, and s is the gradient of the $U_s - U_p$ equation. The pressure P can be written in the form,

$$P = \frac{\rho_0 c_0^2 \eta}{(1 - s\eta)^2} \left(1 - \frac{\Gamma_0 \eta}{2} \right) + \Gamma_0 \rho_0 E_m. \quad (10)$$

The parameters employed in the $U_s - U_p$ EOS are summarised in Table 6.

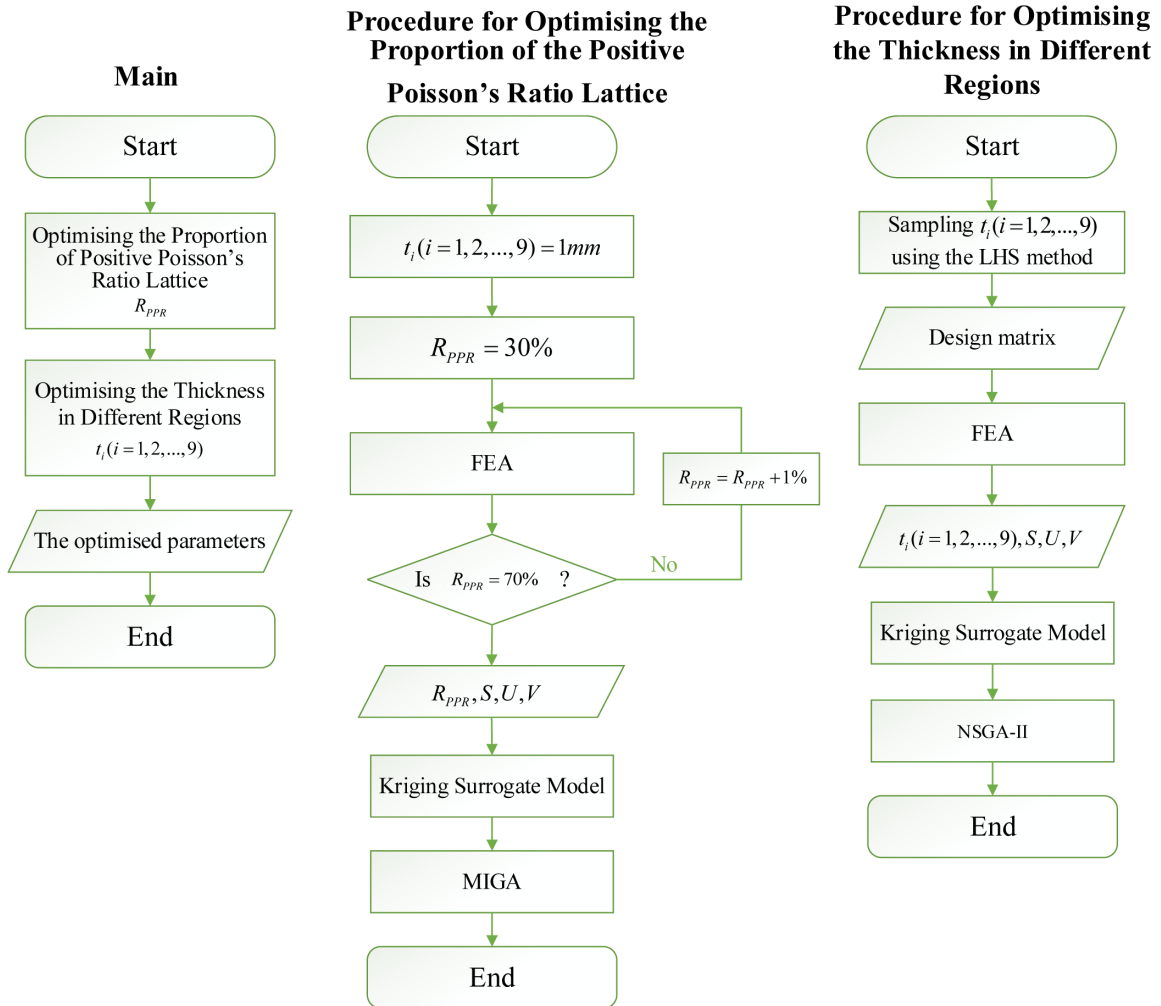
The complete computational model is shown in Figure 2. The blade rotates at 1,500 rpm, and the bird impacts axially at 70 m/s at mid-span (50% of the blade length). Two bird sizes were modelled; their properties are listed in Table 7.

3.4 Optimisation calculations

Owing to the number and complexity of design variables, the optimisation was performed in two stages to improve convergence. Different values of R_{PPR} produce distinct

Table 7. The size of the bird.

Type	Weight (kg)	L_{Bird} (mm)	Φ_{Bird} (mm)	Total number of elements	Total number of nodes
Small	0.35	120	40	2816	3375
Big	2.5	140	60	8256	9229

**Fig. 3.** Schematic of the blade-parameter optimization procedure, showing the steps for proportioning the positive/negative Poisson's ratio lattice and adjusting regional wall thickness.

geometric/topological infill configurations, so topology and thickness should be optimised separately. For simplicity, Stage 1 therefore focuses on topology, while Stage 2 performs thickness optimisation with the topology held fixed. In the first stage, all wallboard thicknesses were fixed at 1.0 mm while the proportion of positive-Poisson-ratio lattice, R_{PPR} , was parametrically sampled from 30% to 70% at 1% intervals. Based on these simulations, a Kriging surrogate model was constructed to represent the mapping from R_{PPR} (and other design inputs) to the objective(s). The Multi-Island Genetic Algorithm (MIGA) was used to optimise the Kriging surrogate with respect to the chosen objective function (see below). This

two-step surrogate-assisted approach significantly reduces computational cost while improving model convergence and robustness.

Use a weighted objective that balances structural performance, energy absorption and mass. In plain text:

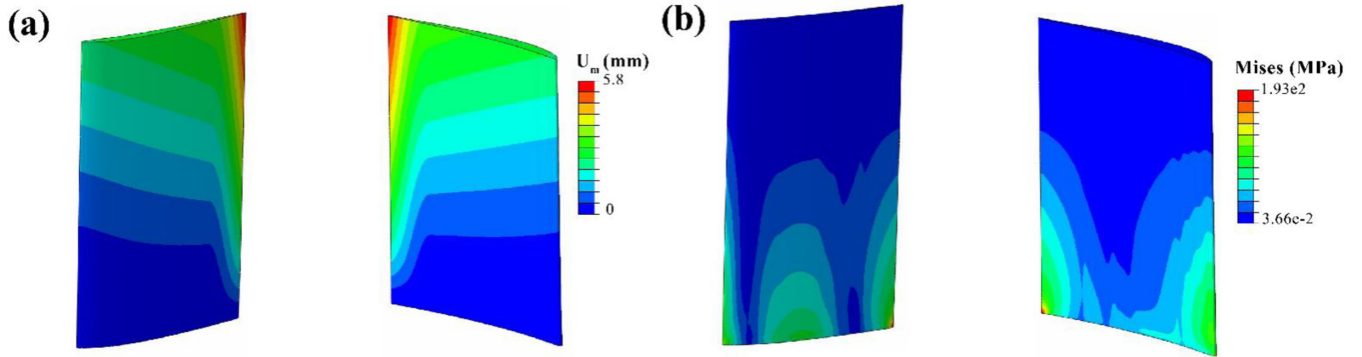
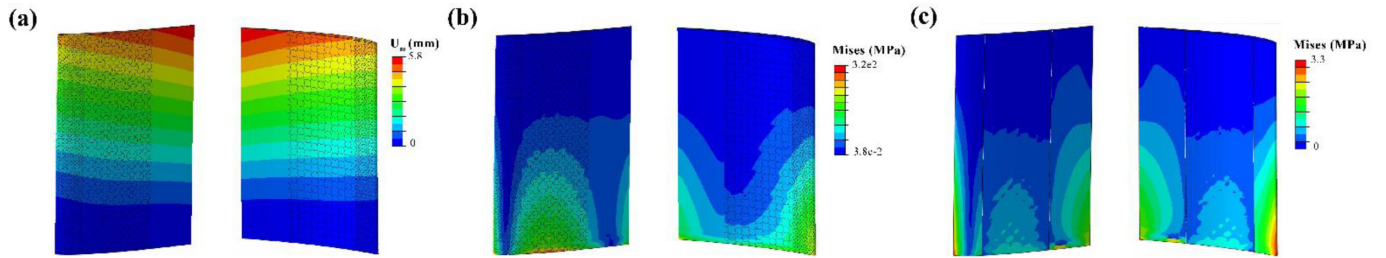
$$\min f = w_1 U + w_2 S + w_3 V \quad (11)$$

where U is deformation, S is stress, and V is the volume. $w_1 = 1.2$, $w_2 = 1.2$, $w_3 = 1$.

This transforms the multi-objective problem into one objective to minimise. As is standard, each weight reflects the relative importance of its objective. By varying the

Table 8. List of design parameters used in the optimisation of the turbofan blade with MPRSH infill structure.

Stage	Region 1a, Region 1b	Region 2a, Region 2b	Region 3a, Region 3b	Region 4	Region 5	Region 6	Region 7	Region 8	Region 9	$\frac{HPR}{t_{profile}}$
	t_1 (mm)	t_2 (mm)	t_3 (mm)	t_4 (mm)	t_5 (mm)	t_6 (mm)	t_7 (mm)	t_8 (mm)	t_9 (mm)	R_{PPR} (%)
I	1	1	1	1	1	1	1	1	1	58.7
II	3	2	0.97	0.83	1.31	3	0.98	2.05	0.77	58.7

**Fig. 4.** Results for the solid-filled blade. (a) Displacement; (b) von Mises stress.**Fig. 5.** The static results for the MPRSHF turbofan blade with PA infill after the first optimization. (a) Displacement. (b) von Mises stress of the whole blade. (c) von Mises stress of the matrix.

weights, one can trace out Pareto-optimal trade-off solutions, since giving a larger weight to an objective biases the solution toward minimising that metric. In practice, equation normalised the scales of U , S , and V so that the weights directly encode their trade-offs, ensuring that no single objective dominates simply due to units or magnitude differences.

In the second stage, Latin Hypercube Sampling (LHS) was employed to generate training samples for the Kriging surrogate, sampling the thickness variables t_i ($i = 1, 2, \dots, 9$). A total of 500 sample sets were generated and used to train the Kriging surrogate model. The multi-objective NSGA-II algorithm was then applied to optimise all wall-panel thicknesses using the surrogate. The full optimisation workflow is illustrated in Figure 3.

4 Results and discussion

4.1 Optimisation results

The final blade parameters after optimisation are listed in Table 8.

4.2 Static structure analysis

To provide a baseline for comparison, a solid-filled blade was simulated under the same loading and boundary-condition set-up as the MPRSHF turbofan blade. The results are presented in Figure 4.

The results of the first optimization are shown in Figure 5. The optimized blade mass is 1.32 kg, representing a 35.0% reduction compared to the solid-filled blade. The maximum displacement is 5.8 mm, which is comparable to that of the solid-filled reference. However, the maximum equivalent stress increased to 320 MPa, representing a 39.7% increase compared to the solid-filled case.

The results of the final optimization are shown in Figure 6. After optimization, the blade mass is 1.66 kg, representing a 20.5% increase relative to the initial optimization and an 18.1% reduction compared with the solid-filled baseline. The maximum displacement decreased to 4.7 mm, a 19.0% reduction relative to both the initial optimization and the solid blade. The peak equivalent stress is 230 MPa, a 28.1% decrease compared with the initial optimization result but a 16.1% increase relative to

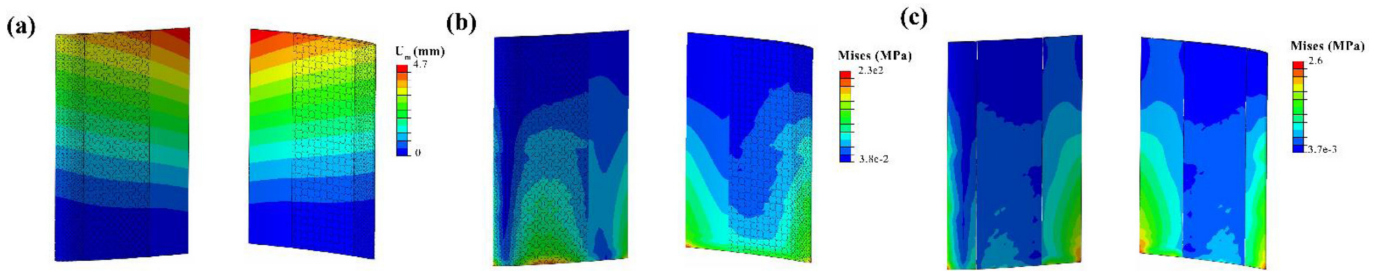


Fig. 6. The static results for the MPRSHF turbfan blade with PA infill after the second optimisation. (a) Displacement. (b) von Mises stress of the whole blade. (c) von Mises stress of the matrix.

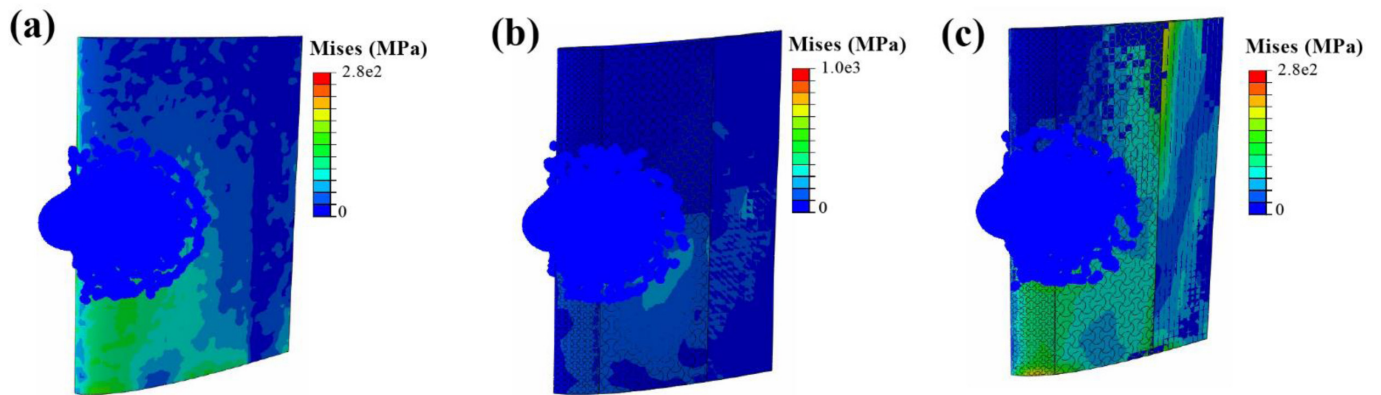


Fig. 7. von Mises stress at the instant of small-bird impact. (a) Solid-filled blade; (b) PA-filled MPRSHF blade; (c) Rubber-filled MPRSHF blade.

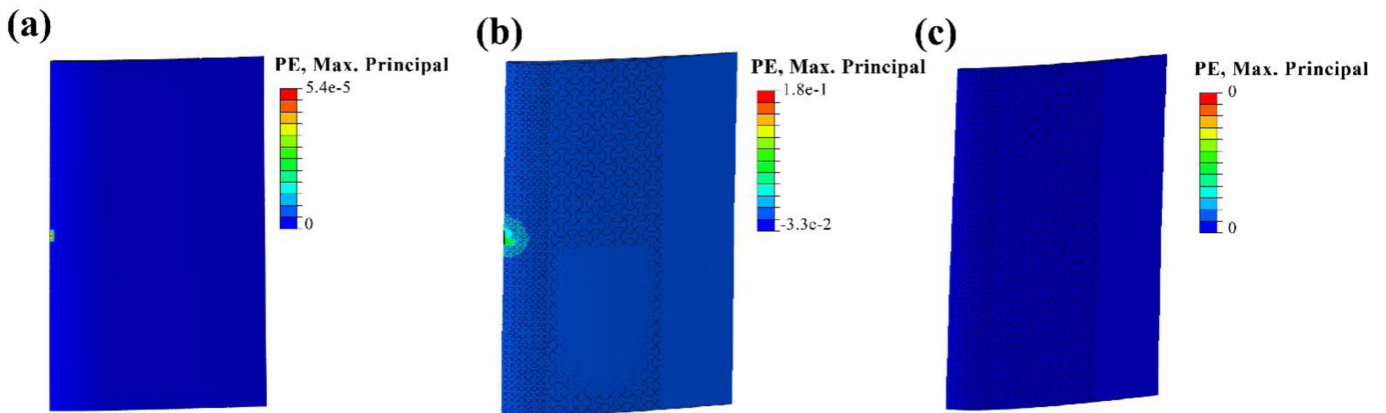


Fig. 8. Plastic strain after small-bird impact: (a) Solid-filled blade. (b) PA-filled MPRSHF blade. (c) Rubber-filled MPRSHF blade.

the solid baseline. Given the TC4 yield strength of 895 MPa, the static strength safety factor for the blade is 3.89, which satisfies the static strength design requirement.

4.3 Bird strike analysis

Figure 7 shows von Mises stress contours at the instant of the small-bird impact. Maximum stresses occur at the impact site and at the blade root, reflecting the combined effects of direct contact loading and bending induced by the impact. The solid-filled and rubber-filled MPRSHF blades

show relatively uniform stress fields, whereas the PA-filled MPRSHF blade exhibits a pronounced, highly localised stress concentration at the impact point, reaching approximately 1000 MPa—substantially higher than in the other two configurations.

Figure 8 presents equivalent plastic-strain contours after the small-bird impact. The PA-filled MPRSHF blade shows substantially larger plastic strains at the impact site than the other two configurations. The solid-filled blade exhibits only a trace plastic strain ($5.4e-5$) and no visible damage, while the rubber-filled MPRSHF blade

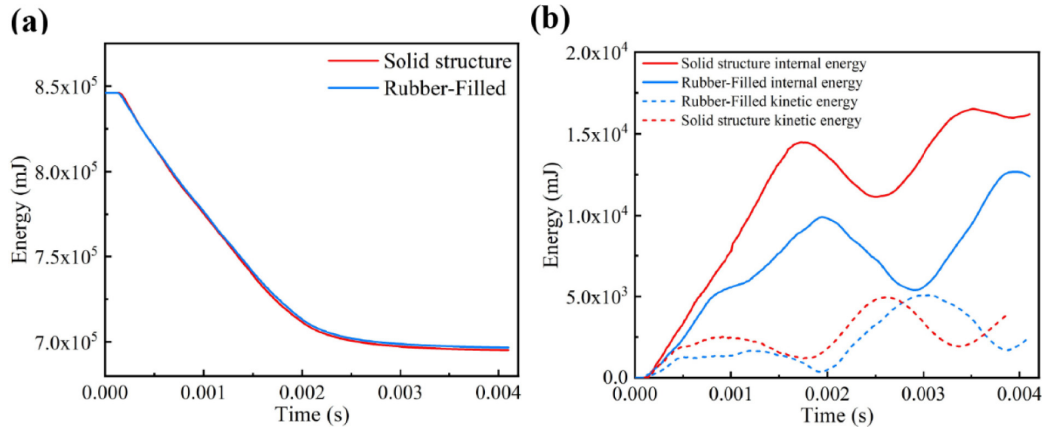


Fig. 9. Time history of energy during the small-bird impact. (a) Kinetic energy of the bird. (b) Internal and kinetic energy of the blade.

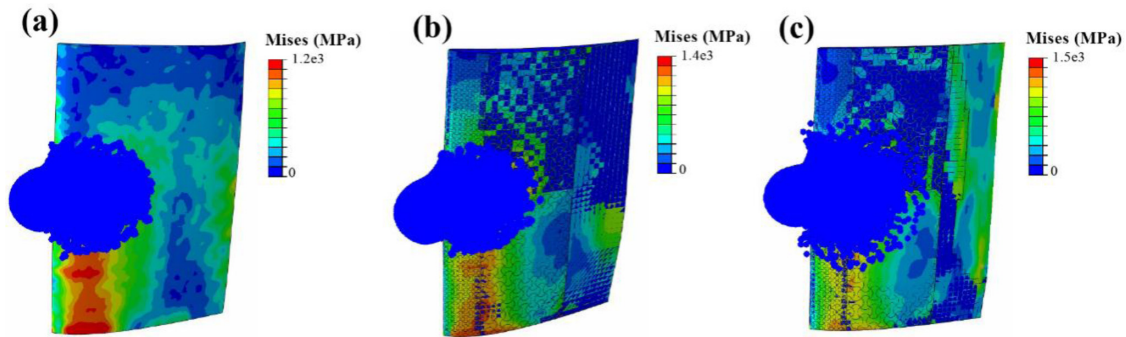


Fig. 10. von Mises stress at the instant of big-bird impact. (a) Solid-filled blade. (b) PA-filled MPRSHF blade. (c) Rubber-filled MPRSHF blade.

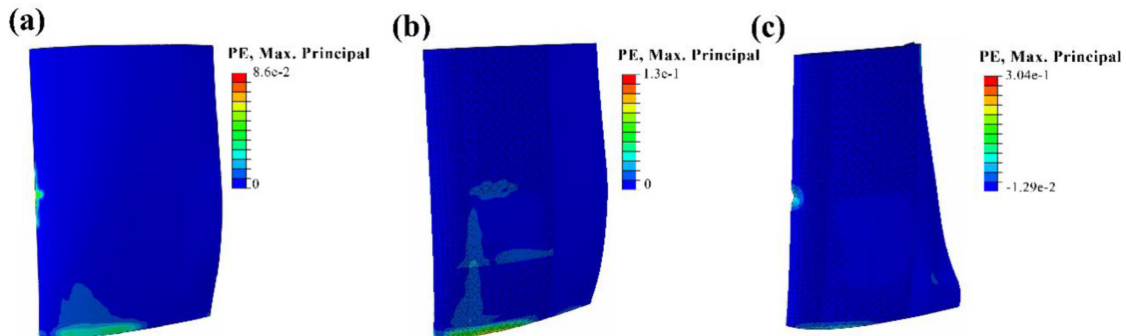


Fig. 11. Plastic strain after big-bird impact. (a) Solid-filled blade. (b) PA-filled MPRSHF blade. (c) Rubber-filled MPRSHF blade.

shows essentially zero plastic strain and no damage. By contrast, the PA-filled MPRSHF blade displays marked local damage at the impact location.

To further examine the MPRSHF blade’s mechanical response, Figure 9 plots the time histories of energy during the small-bird impact. In Figure 9a, the bird retains more kinetic energy after striking the MPRSHF blades than after striking the solid-filled blade, indicating reduced energy transfer to the blade from the bird. In Figure 9b, the solid-filled blade absorbs more total internal energy than the rubber-filled MPRSHF blade, primarily because the solid-filled configuration develops plastic strain and thus dissipates

more kinetic energy via plastic work. However, during the initial (mostly elastic) stage of impact, the rubber-filled MPRSHF blade absorbs more energy than the solid-filled blade. Moreover, the rubber-filled MPRSHF configuration converts a larger fraction of the absorbed internal energy into blade kinetic energy during the impact, consistent with its higher toughness and elastic-energy-storage capability.

To investigate different impact scenarios and the mechanical response of MPRSHF blades, a large bird impact case was considered. Figure 10 shows von Mises stress contours at the instant of impact: under the large-bird impact, all blade configurations exhibit relatively

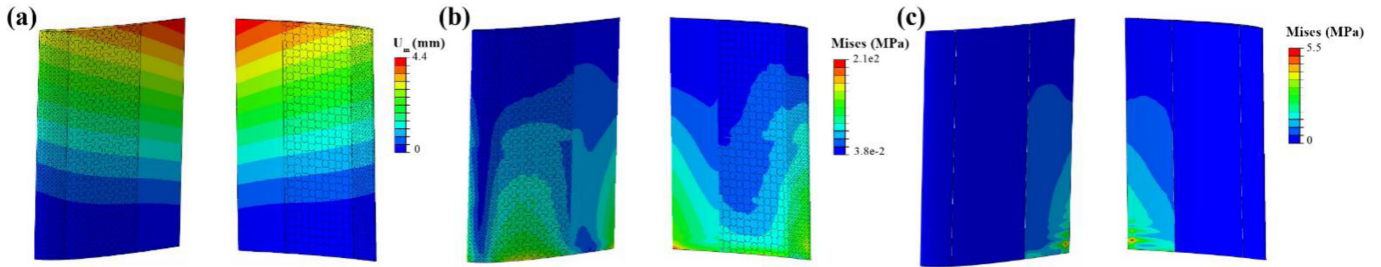


Fig. 12. The static results for the improved MPRSHF Blade. (a) Displacement. (b) von Mises stress of the whole blade. (c) von Mises stress of the matrix.

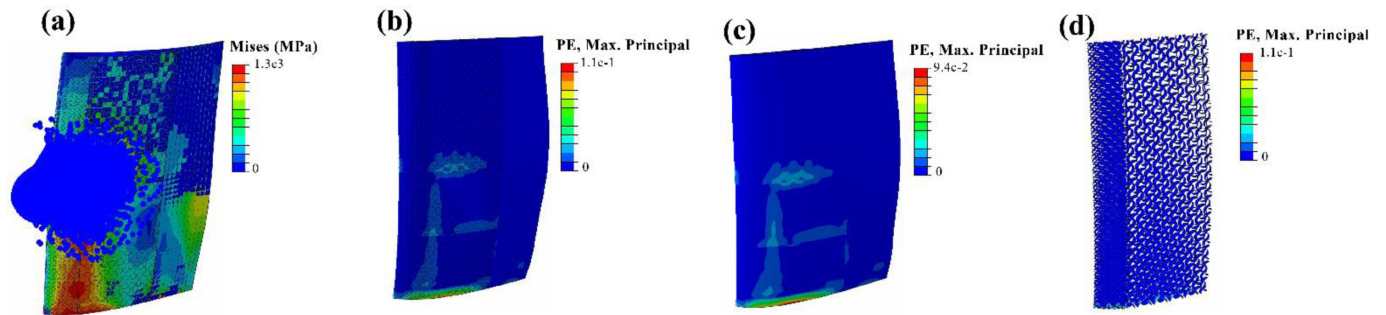


Fig. 13. The big-birds impact results for the improved MPRSHF Blade. (a) von Mises stress of the whole blade. (b) Plastic strain of the whole blade. (c) Plastic strain of the outer shell. (d) Plastic strain of the lattice.

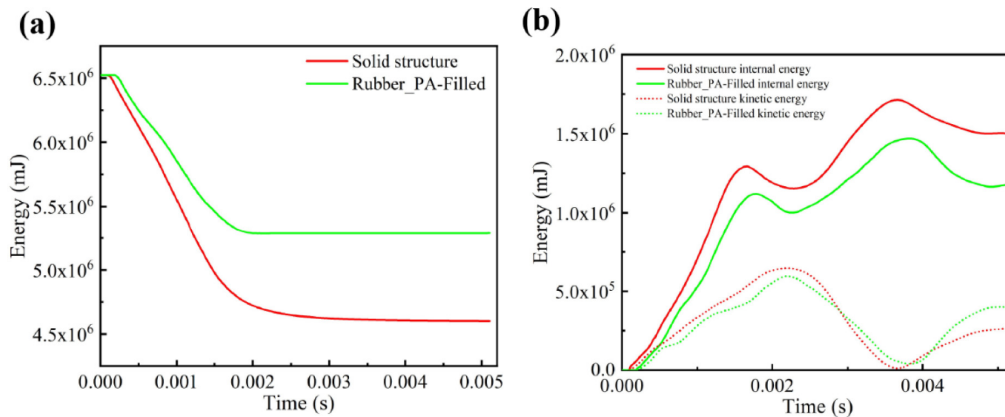


Fig. 14. Time history of energy during the large-bird impact for the improved MPRSHF blade. (a) bird kinetic energy. (b) blade internal and kinetic energy.

uniform stress fields compared with the small-bird case. Figure 11 presents equivalent plastic-strain distributions after the large-bird impact. Because the large bird has greater mass and volume than the small bird, the local stress concentration at the contact point is reduced, while bending loads transmitted to the blade are larger. As a result, the rubber-filled MPRSHF blade experiences catastrophic failure in the trailing-region filler, having exceeded the strength of the rubber material.

4.4 Improved blade with MPRSH infill structure

To address the insufficient strength of the rubber in the blade’s trailing region while exploiting the rubber’s high

toughness and elastic-energy-storage capacity, an improved MPRSHF blade was developed with PA filling in the trailing region and rubber integrated into the lattice metamaterial. The static results for the improved MPRSHF blade are shown in Figure 12. The improved blade’s maximum displacement is 4.4 mm, 6.4% lower than that of the previous MPRSHF design, and its maximum von Mises stress is 210 MPa, a reduction of 8.7% relative to the previous MPRSHF case. Using the TC4 yield strength of 895 MPa, the static safety factor at the critical point is approximately 4.26, indicating a substantial static-strength margin.

The large-bird impact case was used to assess the mechanical response of the improved MPRSHF blade.

Results are presented in Figure 13. As Figures 13a and 13b show, the improved configuration exhibits a relatively uniform stress field and substantially lower stress and plastic-strain levels than both the PA-filled and rubber-filled MPRSHF blades. Figures 13c and 13d indicate that the maximum plastic strain now occurs at the blade root, with little visible damage at the impact site. These results demonstrate that strengthening the trailing-region infill (PA) while integrating rubber into the lattice metamaterial effectively combines the toughness and energy-storage benefits of rubber with the strength of PA, reducing localised impact damage.

Figure 14 shows the time history of energy during the large-bird impact for the improved MPRSHF blade. The improved design reduces the energy transferred from the bird to the blade, and this reduction is more pronounced than in the small-bird impact case. This behaviour stems from the Poisson's ratio mismatch between different lattice regions: the response enables the blade to adapt its deformation under impact, thereby limiting load transmission to the shell and reducing damage. Consistent with earlier observations, the solid-filled blade absorbs more total internal energy than the improved MPRSHF configuration because plastic work in the solid case dissipates more kinetic energy. The improved MPRSHF blade, however, converts a larger fraction of the absorbed internal energy into blade kinetic energy, which helps redistribute and dissipate impact energy and thus better protects the blade structure.

5 Conclusion

This paper presented a bioinspired design and two-stage surrogate-assisted optimisation methodology for wide-chord hollow turbofan blades filled with Multi-Poisson's Ratio Soft-Hard integrated structures. The approach that includes parametric topology sampling, Kriging surrogate construction and evolutionary optimisation of regional thicknesses produced practical designs that balance mass, stiffness and impact survivability.

Quantitatively, the final optimised MPRSHF blade achieves an 18.1% mass reduction versus a solid-filled baseline, a maximum displacement of 4.7 mm ($\approx 19\%$ lower than the initial design and the baseline) and a peak von Mises stress of 230 MPa (safety factor ≈ 3.9 for Ti-6Al-4V). Bird-strike simulations show contrasting behaviours: PA cores produce highly localised stress and plasticity under small-bird impact, rubber fillers limit local plasticity but may fail under large-bird loading, and an improved hybrid (PA trailing fill + rubber-integrated lattice) reduces peak stress to 210 MPa and displacement to 4.4 mm while markedly lowering visible damage.

For practical deployment, several manufacturing and applicability issues must be addressed. Multi-material graded infills pose challenges in material compatibility (thermal expansion and chemical compatibility between metal lattices and polymer/rubber matrices), interface bonding and long-term durability at operating temperatures. Additive manufacturing constraints—minimum printable feature size, surface finish, and build orientation—limit achievable lattice geometries and may necessi-

tate design modifications or hybrid manufacturing (e.g. metal lattice fabrication plus post-fill of compliant matrix). Residual stresses, heat treatment requirements for TC4, and non-destructive inspection of complex internal architectures also require consideration. We therefore recommend incorporating manufacturability constraints (feature-size limits, interfacial design rules, and process-specific material models) into the optimisation loop and exploring hybrid production routes and interfacial treatments to ensure robust bonding.

The proposed methodology is transferable to alternative blade materials and sizes, but designs must be recalibrated for material- and scale-dependent behaviour. For example, nickel-base superalloys or composite shells will change stiffness, strength, and high-temperature performance, while geometric scaling alters local lattice mechanics and dynamic response. Consequently, lattice topology, Poisson-ratio targets and thickness distributions should be re-optimised for each material system and scale, and validated experimentally under representative thermal and impact conditions.

In future work, we will pursue manufacturability-aware optimisation, experimental validation of selected MPRSHF prototypes (including repeated-impact and fatigue testing), and parametric studies over wider Poisson-ratio ranges, impact angles and blade scales to further mature the concept for practical turbofan applications.

Acknowledgments

The authors acknowledge funding from the National Natural Science Foundation of China (Grant No. 52475284).

Funding

This work was supported by the National Natural Science Foundation of China (Grant No. 52475284).

Conflicts of interest

The authors declare no conflict of interest.

Data availability statement

Data will be made available on request

Author contribution statement

Peijie Sun: Conceptualisation, Investigation, Methodology, Software, Validation, Visualisation, Writing - original draft.

Weizhu Yang: Conceptualisation, Methodology, Supervision, Validation, Resources, Writing - review & editing.

References

1. B.L. Koff, Gas turbine technology evolution: a designers perspective, *J. Propuls. Power* **20**, 577 (2004), <https://doi.org/10.2514/1.4361>

2. J. St Peter, *History of aircraft gas turbine development in the US* (ASME, New York, 2002)
3. K.C. Weston, *Energy conversion* (USA: PWS Publishing Company, Boston, MA, 1992)
4. L.M. Amoo, On the design and structural analysis of jet engine fan blade structures, *Prog. Aerosp. Sci.* **60**, 1 (2013), <https://doi.org/10.1016/j.paerosci.2012.08.002>
5. L.S. Langston, G. Opdyke, E. Dykewood, Introduction to gas turbines for non-engineers, *Global Gas Turbine News* **37**, 1 (1997)
6. S. Abrate, Soft impacts on aerospace structures, *Prog. Aerosp. Sci.* **81**, 1 (2016), <https://doi.org/10.1016/j.paerosci.2015.11.005>
7. R. Hedayati, M. Sadighi, M. Mohammadi-Aghdam, On the difference of pressure readings from the numerical, experimental and theoretical results in different bird strike studies, *Aerosp. Sci. Technol.* **32**, 260 (2014), <https://doi.org/10.1016/j.ast.2013.10.008>
8. X. Chen, J. Liu, C. Jiang, Z. Zhao, H. Zhang, C. Zhang, Y. Li, Evaluation of a substitute bird for engine fan blade impact tests considering the bird-slicing state, *Eng. Fail. Anal.* **167**, 109056 (2025), <https://doi.org/10.1016/j.engfailanal.2024.109056>
9. V. Merculov, M. Kostin, G. Martynenko, N. Smetankina, V. Martynenko, Force simulation of bird strike issues of aircraft turbojet engine fan blades, in: *International Conference on Reliable Systems Engineering*, Springer, 2021, pp. 129–141, https://doi.org/10.1007/978-3-030-83368-8_13
10. S. Wang, C. Jiang, C. Wang, B. Zhang, H. Luo, W. Feng, Bird strike resistance analysis for engine fan blade filled with triply periodic minimal surface, *Aerosp. Sci. Technol.* **161**, 110109 (2025), <https://doi.org/10.1016/j.ast.2025.110109>
11. B. Han, Z.-J. Zhang, Q.-C. Zhang, Q. Zhang, T.J. Lu, B.-H. Lu, Recent advances in hybrid lattice-cored sandwiches for enhanced multifunctional performance, *Extreme Mech. Lett.* **10**, 58 (2017), <https://doi.org/10.1016/j.eml.2016.11.009>
12. X. Zhang, W. Yanrong, C. Weiyu, X. Jiang, Parametric study on the flutter sensitivity of a wide-chord hollow fan blade, *Chin. J. Aeronaut.* **35**, 277 (2022)
13. Z. Chuan, J. Xiang-hua, C. Xiang-hai, S. Tong-cheng, TC4 hollow fan blade structural optimization based on bird-strike analysis, *Proc. Eng.* **99**, 1385 (2015), <https://doi.org/10.1016/j.proeng.2014.12.674>
14. Y. Zhang, Y. Zhou, Investigation of bird-strike resistance of composite sandwich curved plates with lattice/foam cores, *Thin-Walled Struct.* **182**, 110203 (2023), <https://doi.org/10.1016/j.tws.2022.110203>
15. E. Giannaros, A. Kotzakolios, V. Kostopoulos, G. Sotiriadis, R. Vignjevic, N. Djordjevic, M. Boccaccio, M. Meo, Low-and high-fidelity modeling of sandwich-structured composite response to bird strike, as tools for a digital-twin-assisted damage diagnosis, *Int. J. Impact Eng.* **160**, 104058 (2022), <https://doi.org/10.1016/j.ijimpeng.2021.104058>
16. Y. Jun, C. Zhang, H. Sixu, C. Xianghai, L. Zhihui, Y. Kun, Experimental and numerical simulation of bird-strike performance of lattice-material-infilled curved plate, *Chin. J. Aeronaut.* **34**, 245 (2021), <https://doi.org/10.1016/j.cja.2020.09.026>
17. R. Hedayati, M. Sadighi, Effect of using an inner plate between two faces of a sandwich structure in resistance to bird-strike impact, *J. Aerosp. Eng.* **29**, 04015020 (2016), [https://doi.org/10.1061/\(ASCE\)AS.1943-5525.0000505](https://doi.org/10.1061/(ASCE)AS.1943-5525.0000505)
18. Y. Zhu, X. Wu, X. Rui, D. Gan, Q. Wang, C. Zhang, On the design and in-plane crashworthiness of a novel extendable assembled auxetic honeycomb, *Thin-Walled Struct.* **211**, 113123 (2025), <https://doi.org/10.1016/j.tws.2025.113123>
19. J. Li, C. Sui, Y. Sang, Y. Zhou, Z. Zang, Y. Zhao, X. He, C. Wang, A flexible, reusable and adjustable high-performance energy absorption system inspired by interlocking suture structures, *Int. J. Solids Struct.* **296**, 112839 (2024), <https://doi.org/10.1016/j.ijsolstr.2024.112839>
20. F. Lu, T. Wei, C. Zhang, Y. Huang, Y. Zhu, X. Rui, A novel 3D tetra-missing rib auxetic meta-structure with tension/compression-twisting coupling effect, *Thin-Walled Struct.* **199**, 111764 (2024), <https://doi.org/10.1016/j.tws.2024.111764>
21. T. Wei, F. Lu, C. Zhang, Y. Huang, X. Rui, Y. Zhu, Energy absorption of 3D assembled auxetic meta-structure with compression-twisting effect, *Structures* **73**, 108482 (2025), <https://doi.org/10.1016/j.istruc.2025.108482>
22. C. Zhang, F. Lu, T. Wei, H. Wang, F. Liu, Y. Zhu, Windmill-shaped metamaterials achieving negative thermal expansion, *Eng. Struct.* **336**, 120488 (2025), <https://doi.org/10.1016/j.engstruct.2025.120488>
23. The stomatopod dactyl club: A formidable damage-tolerant biological hammer, *Science* **336**, 1275 (2012), <https://doi.org/10.1126/science.1218764>
24. S.N. Patek, R.L. Caldwell, Extreme impact and cavitation forces of a biological hammer: Strike forces of the peacock mantis shrimp *odontodactylus scyllarus*, *J. Exp. Biol.* **208**, 3655 (2005), <https://doi.org/10.1242/jeb.01831>
25. A. Ingrole, T.G. Aguirre, L. Fuller, S.W. Donahue, Bioinspired energy absorbing material designs using additive manufacturing, *J. Mech. Behav. Biomed. Mater.* **119**, 104518 (2021), <https://doi.org/10.1016/j.jmbbm.2021.104518>
26. J. McKittrick, P.-Y. Chen, L. Tombolato, E.E. Novitskaya, M.W. Trim, G.A. Hirata, E.A. Olevsky, M.F. Horstemeyer, M.A. Meyers, Energy absorbent natural materials and bioinspired design strategies: a review, *Mater. Sci. Eng.: C* **30**, 331 (2010), <https://doi.org/10.1016/j.msec.2010.01.011>
27. F. Barthelat, H. Tang, P. Zavattieri, C. Li, H. Espinosa, On the mechanics of mother-of-pearl: a key feature in the material hierarchical structure, *J. Mech. Phys. Solids* **55**, 306 (2007), <https://doi.org/10.1016/j.jmps.2006.07.007>
28. F. Barthelat, R. Rabiei, Toughness amplification in natural composites, *J. Mech. Phys. Solids* **59**, 829 (2011), <https://doi.org/10.1016/j.jmps.2011.01.001>
29. Z. Jia, Y. Yu, S. Hou, L. Wang, Biomimetic architected materials with improved dynamic performance, *J. Mech. Phys. Solids* **125**, 178 (2019), <https://doi.org/10.1016/j.jmps.2018.12.015>
30. W. Yang, Q. Liu, Z. Gao, Z. Yue, B. Xu, Theoretical search for heterogeneously architected 2D structures, *Proc. Natl. Acad. Sci.* **115**, E7245 (2018), <https://doi.org/10.1073/pnas.1806769115>
31. W. Yang, Q. Liu, Z. Yue, X. Li, B. Xu, Rotation of hard particles in a soft matrix, *J. Mech. Phys. Solids* **101**, 285 (2017), <https://doi.org/10.1016/j.jmps.2017.01.008>
32. A.G. Thomas, J.M. Whittle, Tensile rupture of rubber, *Rubber Chem. Technol.* **43**, 222 (1970), <https://doi.org/10.5254/1.3547249>
33. W. Yang, Z. Gao, Z. Yue, X. Li, B. Xu, Hard-particle rotation enabled soft-hard integrated auxetic mechanical metamaterials, *Proc. Royal Soc. A: Math. Phys. Eng. Sci.* **475**, 20190234 (2019), <https://doi.org/10.1098/rspa.2019.0234>

34. H. Zhang, W. Yang, Q. Liu, Y. Gao, Z. Yue, B. Xu, Mechanical janus structures by soft-hard material integration, *Adv. Mater.* **35**, 2370037 (2023). <https://doi.org/10.1002/adma.202370037>
35. W. Yang, S. Dong, X. Zhu, S. Ren, L. Li, Superior energy absorption performance of layered aux-hex honeycomb filled tubes, *Int. J. Mech. Sci.* **234**, 107702 (2022), <https://doi.org/10.1016/j.ijmecsci.2022.107702>
36. C. Guo, L. Huang, K. Tian, Combinatorial optimization for UAV swarm path planning and task assignment in multi-obstacle battlefield environment, *Appl. Soft Comput.* **171**, 112773 (2025), <https://doi.org/10.1016/j.asoc.2025.112773>
37. L. Huang, Y. Zuo, C. Guo, B. Wang, K. Tian, Machine learning in flight parameter-based structural load prediction: a review and framework proposal, *Prog. Aerosp. Sci.* **159**, 101145 (2025), <https://doi.org/10.1016/j.paerosci.2025.101145>
38. P. Sun, W. Yang, Y. Zhang, B. Zhang, Z. Fan, L. Li, Enhanced tensile properties of 3D printed soft-hard composites due to poisson's ratio mismatch: experimental and numerical study, *Compos. Part B: Eng.* **299**, 112413 (2025), <https://doi.org/10.1016/j.compositesb.2025.112413>
39. V. Merculov, M. Kostin, G. Martynenko, N. Smetankina, V. Martynenko, Force simulation of bird strike issues of aircraft turbojet engine fan blades, in *International Conference on Reliable Systems Engineering (ICoRSE) - 2021 (ICoRSE 2021)*, Springer, 2021, pp. 129–141. https://link.springer.com/chapter/10.1007/978-3-030-83368-8_13
40. Y. Zhu, *Simulation study of multi-bird impact damage of an Aero-engine fan blade* The Professional Degree of Master of Engineering, Civil Aviation University of China, 2022
41. X. Zhang, P. Sun, Y. Zhang, F. Wang, Y. Tu, Y. Ma, C. Zhang, Design and optimization of 3D-printed variable cross-section I-beams reinforced with continuous and short fibers, *Polymers* **16**, 684 (2024), <https://doi.org/10.3390/polym16050684>
42. X. Jiang, *Simulation analysis of the hysteresis heat generation in damping rubber*, Master of Engineering, Xiangtan University, 2020
43. G.R. Johnson, W.H. Cook, Fracture characteristics of three metals subjected to various strains, strain rates, temperatures and pressures, *Eng. Fract. Mech.* **21**, 31 (1985), [https://doi.org/10.1016/0013-7944\(85\)90052-9](https://doi.org/10.1016/0013-7944(85)90052-9)
44. R.H. Mao, S.A. Meguid, T.Y. Ng, Finite element modeling of a bird striking an engine fan blade, *J. Aircraft* **44**, 583 (2007), <https://doi.org/10.2514/1.24568>
45. T. Brockman, T.W. Held, *Explicit finite element method for transparency impact analysis*, 1991. <https://api.semanticscholar.org/CorpusID:106679372>

Cite this article as: Peijie Sun, Weizhu Yang, Design and optimisation of a turbofan blade filled with Multi-Poisson's Ratio Soft-Hard integrated structures, *EPJ Appl. Metamat.* **13**, 7 (2026), <https://doi.org/10.1051/epjam/2025015>